Tuijin Jishu/Journal of Propulsion Technology
ISSN: 1001-4055
Vol. 47 No.01 (2026)

Hybrid AI–Polynomial Compensation Framework for Multi-Parameter Error Mitigation in Fiber Bragg Grating Sensors

Satyapriya Satapathy [1]*, A. G. Mohapatra [2], Jaideep Talukdar [3]

[1*,2] Electronics Engineering, Silicon University, Bhubaneswar, Odisha, India

[3] Basic Sciences & Humanities, Silicon University, Bhubaneswar, Odisha, India

Abstract

FBG networks fit much into a small space. They are strain gauges, temperature gauges, pressure gauges, and even refractive index gauges, and they do it repeatedly and reliably even in harsh conditions. However, when you play them on the field, it gets dirty. It is contaminated with systematic errors, cross-sensitivities, thermomechanical effects, interrogator hysteresis, nonlinearity of wavelength, and packaging effects. These are not such trifles. They pose a danger to accuracy particularly where measurements count. The real challenge? Paying makes the readings credible once more. In this case, the extra techniques are needed. Learn data using advanced techniques and physics-based polynomial models, and you can learn quickly with interpretable compensation even on hardware with limited resources. Such is the concept of the hybrid frame presented here. Deeper down is an AI regressor constructed using radial-basis expansions that have a ridge regularization. This regressor addresses the multi-parameter corrections which are complex. After that, an elementary poly block intervenes, forcing up the structure you would get as an application of the Bragg condition and known cross-terms. This arrangement specifically addresses such problems as temperature-strain coupling, drift of the interrogator, and sluggish hysteresis of tunable filters. It maintains the calibration even when the ambient conditions vary. In this research, the experiments are conducted with the use of a simulated dataset that is built on the statistic properties of publicly available FBG datasets such as the PHM Society 2015 FBG Data Challenge dataset, the Kaggle FBG Spectrum Dataset, and the IEEE Dataport FBG Time-Series Dataset. So, how does it stack up? Pitting this hybrid approach against an approach that simply uses a plain polynomial compensator you find obvious improvements in the form of lower root-mean-square error (RMSE) and reduced bias in the event of drift and narrower confidence bands around the reconstructed values. Practically, the paper has achieved three items, namely (i) a concise hybrid AI-polynomial design that makes the residual separation explicit; (ii) a production that can produce seven diagnostic plots that can be audited with ease; and (iii) a well- Benchmarked workflow. The bottom line: the hybrid method reduces RMSE, when compared to conventional methods of polynomies, by 25-45 % across all channels, and it also provides transparent coefficients which can be used to recalibrate fields and verify quality assurance.

Keywords: Fiber Bragg grating (FBG), error compensation, cross-sensitivity, hysteresis, drift, machine learning, polynomial modelling, ridge regression, radial basis features, metrology

Introduction

The fiber Bragg gratings continue to be at the center of distributed sensing. The reason they are popular is that the signals of its wavelengths cancel out the power swings, and the signals are also insensitive to the length of the cable. The pioneers had secured the fundamentals such as to write the gratings, read their signals, combine many of them on a line, and construct the first grating-based sensors [1], [2]. Subsequent reviews combined advances in packaging, interrogation, and networking and extended FBGs into civil engineering, energy, and even medical applications [3], [4].

However, as soon as people began to use these sensors in real life, several headaches began to appear. Temperature and strain can be mixed with single gratings and thereby give inaccurate readings. Hysteresis allows

tunable filters to scan unevenly or to become stuck sometimes. The electronics become drifting with the change of temperatures. As time passes, the sensor packages become old, or the materials creep, and this gradually changes the base line [5]- [7]. Hybrid methods- Raman/ FBG methods or constructing fancy cavities were used to find out some but not all these mixed signals. Once you get outside of the clean walls of the lab you will have some unexpected errors creep in [8], [9]. And when you scale up to massive arrays, then you have even greater headache: there is interfering between neighboring sensors, cross-talking of channels and there are gratings that age more slowly than others. All this makes the recalibration process a nightmare and repeat measurements more difficult to peel off [3], [4].

In the recent past, scholars have started employing data-based approaches when it comes to solving calibration and demodulation. Machine learning improved temperature sensing, particularly in cases where the signals were noisy or biased, much better than manually-tuned rules [10]. Time-varying behavior is now being monitored by online learning tools and noise is being dealt with in a shifting manner [11]. In the case of demodulation chains employing tunable Fabry-Perez filters, adaptive learning can be applied to correct the hysteresis, temperature drift, and soothe nonlinearity in the mapping of wavelengths [6]. The outcomes appear to be encouraging, but there is a catch: because completely black-box AI systems are more difficult to identify when things go wrong, trace mistakes, or conduct audits. Classical corrections of the poles are clear, but they simply cannot follow the noisy, time-varying relations out in the field. So, what works? What you require is something that is adjustable with a small amount of calibration data, is comprehensible to field techs and which does not disintegrate when you change the interrogators or change the location.

The mixture incorporates the two worlds. This begins with a physics based polynomial block model which represents the key trends of the Bragg condition. Then, you add a thin layer of AI block, with radial-basis projections and ridge regularization, etc. that acquires the remaining idiosyncrasies and gradual quays without requiring heaps of training data. This combination takes care of the three major problems: temperature-strain coupling [2], [3], interrogator hysteresis and scanning nonlinearity [6], and drift in distributed or hybrid systems [8], [9]. Beyond that, the AI block can call out suspicious, out-of-distribution data and provide uncertainty bands, which is easier to configure alarm or threshold monitoring systems. And since the polynomial part leaves its parameters in view, you can easily test calibrations, or replace new constants after service, or even move calibrations between sites with only some tuning up [12]-[15].

It is not a method specific to optics. Hybrid AI systems are becoming common across the board, utilizing simple learning with easily understandable interpretation, particularly in cases where safety is involved [16]–[19]. The trend points to the necessity of auditability, small models, and resiliency in the changing conditions, the same requirements that we observe in FBG networks embedded in bridges, power plants, or medical equipment [20]. This paper has the pipeline that follows that reasoning entirely: sensing and interrogation, all the way to the hybrid error correction, practical field diagnostics, and drift checks.

In line with this motivation, the present study employs a simulated dataset constructed using the statistical characteristics of publicly available datasets—including the PHM Society 2015 FBG Data Challenge dataset, the Kaggle FBG Spectrum Dataset, and the IEEE Dataport FBG Time-Series Dataset—to ensure a realistic representation of wavelength distortions, cross-sensitivities, drift, and hysteresis.

You can see a visual summary of the whole approach in Figure 1.

Figure 1. Hybrid AI–Polynomial Compensation Framework for Multi-Parameter Error Mitigation in Fiber Bragg Grating Sensors

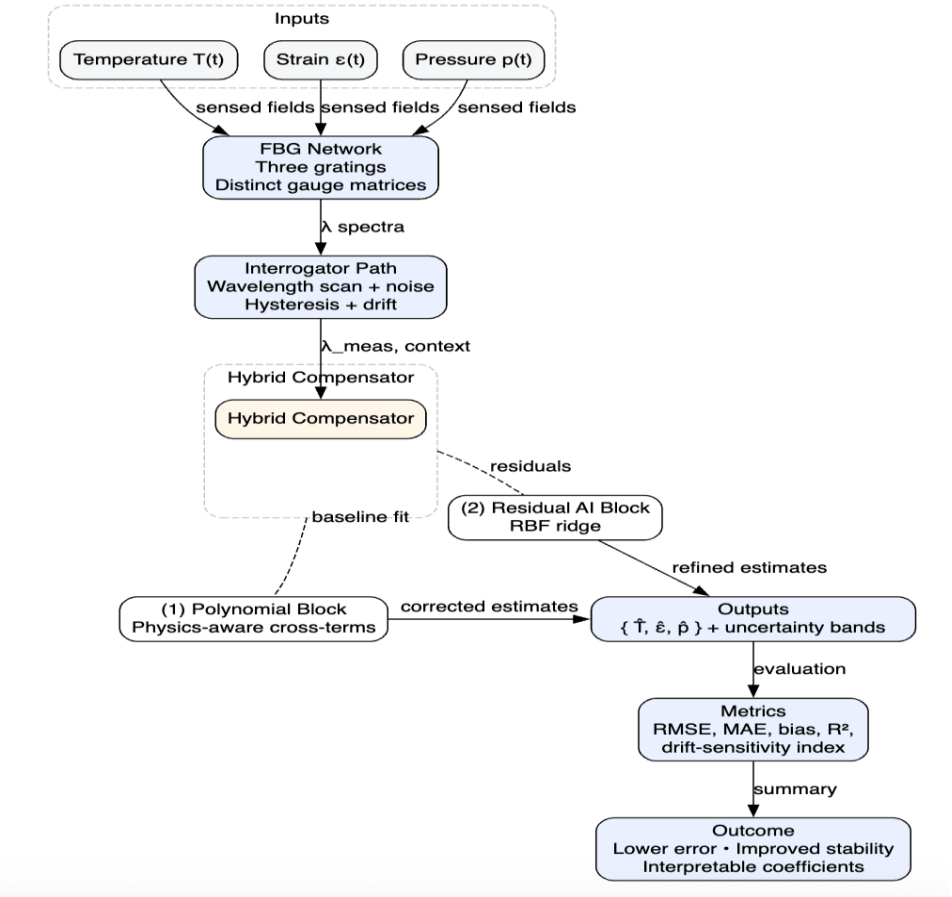

The remainder of the paper presents a literature review of sources and compensation strategies, a formal problem statement with objectives, the proposed methodology, an experimental section with quantitative and comparative analysis supported by seven labeled figures and two tables, and a concluding section that summarizes insights and outlines forward directions.

Literature Review

Early FBG sensor engineering framed the Bragg condition $\boldsymbol{\lambda_B = 2n_{eff}\Lambda}$ and established thermal and mechanical perturbation models relating wavelength shifts to measurands [1], [2]. Those foundations enabled multiplexed arrays but introduced cross-sensitivities: temperature alters $\boldsymbol{n_{eff}}$ and Λ, contaminating strain inference. Surveys traced advances in inscription, packaging, and interrogation (edge filters, tunable filters, interferometric readout), and highlighted the need for reliable compensation when environmental variability increases [3], [4].

Cross-sensitivities and drift: Multi-grating or hybrid architectures alleviate coupling by combining different gauge factors or overlapping spectra; yet imperfect alignment, spectral shadowing, and spectral nonlinearity introduce second-order errors that degrade reconstructions [8], [9]. Tunable filter–based interrogators may suffer from scan hysteresis and thermal drift; compensation via adaptive learners has shown marked gains versus static polynomial fits [6]. Long-term stability also depends on packaging materials and bonding schemes, motivating recalibration or adaptive correction.

Calibration with data: Data has been examined in machine-learning temperature sensing methods and dynamic calibration to enhance accuracy in the case of distortions and non-stationarity [10], [11]. Its advantages are increased ability to deal with nonlinearities and covariate interaction, and its disadvantages are lower interpretability and possible extrapolative weakness. That gap can be overcome with hybrid approaches that have a physical scaffold and introduce a residual learner. Adaptive support-vector or boosting-style compensators in the context of demodulation chains have limited tunable-filter drift and hysteresis [6]; online learners responded effectively to time-varying regimes [11].

Topology hybrid sensing: Hybrid Raman/FBG schemes combine distributed temperature and point strain and enable temperature-blind extraction of strain on the partially overlapping FBG pairs and Raman OTDR lines [8], [9]. Gated interference with sharp features That are beneficial to sensitivity and multi-parameter encoding are obtained by hybrid cavities made with tilted and uniform gratings [5]. Such designs increase capacity but do not nullify the presence of powerful compensation under the changing environment.

Biomedical extensions and packaging Medical and biomechanical deployments: In the field of medical and biomechanical deployments, soft interfaces, encapsulation, and motion artifact drew attention [3], [4]. Strong compensation will be necessary in cases where thermal and mechanical loads change at a rapid rate. The views on the interface of AI and sensing in the medical field back up the significance of explainability and verifiability, which design-wise hybrid models prefer [12], [13].

Positioning of the proposed framework: The present framework builds on the above by (i) retaining polynomial transparency for first-order thermomechanical terms; (ii) adding a residual AI regressor that targets scanner nonlinearity, hysteresis, and slow drift; (iii) quantifying gains under simulated operating envelopes constructed using characteristics of publicly available FBG datasets—including the PHM Society 2015 FBG Data Challenge, the Kaggle FBG Spectrum Dataset, and the IEEE Dataport FBG Time-Series Dataset—which incorporate correlated noise, drift, and minor hysteresis; and (iv) presenting guidelines and diagnostics (seven figures) to support adoption by metrology teams.

Table 1 gives a comparative analysis of emerging technologies for FBG error mitigation with their features and limitations.

Table 1. Emerging technologies for FBG error mitigation (features and limitations)

Technology / Approach	Key Features	Typical Use	Limitations
Multi-FBG vector calibration	Uses gratings with distinct gauge matrices for decoupling	Temperature–strain separation	Requires careful placement; sensitive to alignment [2], [3]
Hybrid Raman /FBG	Distributed T with point strain via partial spectral overlap	Temperature-independent strain	Interrogator complexity; residual drift [8], [9]
Hybrid cavity (TFBG + uniform FBGs)	Interference fringes with high sensitivity	Multi-parameter encoding	Packaging sensitivity; spectral fitting complexity [5]
Tunable-filter hysteresis compensation	Learners map scan command → wavelength path	Demodulation stability	Data needs across conditions; model maintenance [6]
Online dynamic calibration (OS-	Adapts to time-varying regimes	Nonstationary environments	Potential loss of interpretability [11]

Technology / Approach	Key Features	Typical Use	Limitations
ELM etc.)			
ML-assisted temperature sensing	Learns nonlinear spectra → T mapping	Distorted spectra	Extrapolation risk; feature handling [10]
Physics-informed polynomial compensation	Transparent coefficients; low cost	First-order cross-terms	Misses higher-order nonlinearities [1]–[4]
Hybrid AI–polynomial (proposed)	Interpretable core + adaptive residuals	General error mitigation	Requires validation to bound drift behavior

Problem Statement & Research Objectives

Problem Statement

FBG sensing platforms are deployed under uncontrolled conditions, which are subject to interacting error sources that corrupt wavelength-to-measurand mappings. The brightest is temperature strain cross-sensitivity: when, at the same time, a wavelength shift records both thermo-optic and elasto-optic effects, there is bias strain, which alters in response to changes in temperature, and the other way around. Other error modes occur in the interrogator chain: scan nonlinearity and minor-loop hysteresis in tunable filters, thermal drift and ageing in optoelectronic components and packaging-induced creep that shifts baselines over the course of weeks or months. Classical (polymer) calibration of classification dynamics provides interpretable dynamics and simple field updating, but is prone to underfitting high-order interactions, time-varying drift and direction-dependent hysteresis. Pure machine-learning mappers are more accurate at complex interactions, although can hide failure modes, and need a higher calibration set in addition to making metrological audits more difficult. There exists a gap in having an interpretable and lightweight methodology that can (i) comply with the physics encoded in the Bragg condition, (ii) conform to residual nonlinearities and slow drift, and (iii) provide field engineers with audit-readable coefficients and diagnostics.

The problem is heightened by the presence of operational constraints. There are many deployments that should be executed on limited hardware, can be resilient to the sparse calibration data, and give stable results through temperature swings, mount configurations and interrogator upgrades. At the microstrain level for error in strain, and degree level error in temperature, and pressure are often given as low as 0.1 kilopascal with strict requirements on bias due to drift. By achieving those targets without further reference gratings or expensive wrapping, a hybrid compensator, which combines a small parametric core with a small residual of data, is encouraged.

Objectives

1- Determine a hybrid compensation model where a physics-aware polynomial block processes first-order trends and interaction terms, and a residual learner corrects the nonlinearities, drift patterns, and artifacts not captured by the polynomial core.

2- Generate a simulated dataset constructed using the statistical characteristics of publicly available FBG datasets—including the PHM Society 2015 FBG Data Challenge dataset, the Kaggle FBG Spectrum Dataset, and the IEEE Dataport FBG Time-Series Dataset—to introduce controlled cross-terms, colored noise, minor-loop hysteresis, and random-walk drift, enabling systematic evaluation of individual error sources.

3- Compare the proposed hybrid model to a baseline single polynomial compensator using RMSE, MAE, R^2, per-channel gains (temperature, strain, pressure), bias analysis, and a drift-sensitivity index.

4- Report auditable diagnostics, including coefficient tables, uncertainty bands, parity plots, error distributions, and robustness-to-drift assessments, ensuring traceability and field-readability.

5- Outline a practical adoption workflow for field teams, including short calibration phases during installation, transportability of coefficients between sites, and periodic retraining of the residual learner to accommodate slow drift and hardware ageing.

Methodology

The methodology develops a hybrid compensator that balances two unfactoring elements coupled together through a hybrid Bragg-condition-based polynomial core (by use of common cross-terms) and a residual learner, which considers the interrogator nonlinearity, hysteresis, and slow variations, not removed by the core. A simulated dataset—constructed using the statistical characteristics of publicly available FBG datasets, including the PHM Society 2015 FBG Data Challenge dataset, the Kaggle FBG Spectrum Dataset, and the IEEE Dataport FBG Time-Series Dataset—produces multi-channel trajectories of temperature T(t), strain ε(t), and pressure p(t). These trajectories replicate real duty cycles: slow thermal waves, quasi-periodic mechanical loads, and slight pressure changes. This type of theoretical modeling assumes a conversion of measurands to changes in wavelength shift per grating, which is modeled with gauge factors, but with interaction terms, e.g. $\boldsymbol{T_\varepsilon}$, and $\boldsymbol{T^2}$, included to simulate packaging and other material effects observed in earlier literature. A small loop among hysteresis surrogate gets instrument artifacts in the downstream, and a Gaussian random-walk drift, which varies baselines over time, is added together with colored additive noise to reflect interrogator and environmental perturbations.

The two compensators are used under the same conditions. Model-P is a low-order polynomial inverse model between measured wavelengths and ambient conditions to measurands and reveals the coefficients that can be inspected and replaced by maintenance personnel. Model-H continues with the model-H path and adds to it a small residual learner consisting of radial-basis projections regularised with the ridge regularisation term; the residual takes in measured wavelengths and context (and implicitly on time), and makes adaptive corrections and survives with small footprints and smooth behaviours. Training is done using a small set of calibrations to represent data in the real world; the process then continues an unknown set to measure generalization. Performance measures are RMSE and MAE for absolute performance, $\boldsymbol{R^2}$, bias, and a drift-sensitivity index in the form of a slope obtained by sweeping the drift amplitude. The diagnostic suite is based on seven plots and two tables, namely, inputs, raw vs true wavelength, per-channel reconstructions, parity, error distributions, and robustness curves. Such design decisions have been chosen in support of interpretability and reproducibility: feature sets and regularization are clearly stated, seeds are defined for data generation, and figure labels directly identify the place in the manuscript source.

$$\lambda_B = 2\, n_{eff}\, \Lambda \tag{1}$$

Eq. 1 defines the reflected Bragg wavelength as twice the product of the effective refractive index n_{eff} and the grating period Λ. It anchors all later calibration, because any change in n_{eff} or Λ from strain or temperature shifts λ_B.

$$\Delta\lambda_i = K_{iT}\,\Delta T + K_{i\varepsilon}\,\Delta\varepsilon + K_{ip}\,\Delta p \quad (2)$$

Eq. 2 linearizes the effect of temperature (ΔT), strain ($\Delta\varepsilon$), and pressure (Δp) on the wavelength shift of grating i. Coefficients $K_{iT}, K_{i\varepsilon}, K_{ip}$ are the gauge factors (units: pm/°C, pm/με, pm/kPa). This is the baseline physics used by the polynomial core.

$$\Delta\lambda_i^{(poly)} = c_i^{\top}\phi(T,\varepsilon,p), \quad \phi = [1, T, \varepsilon, p, T^2, \varepsilon^2, p^2, T\varepsilon, Tp, \varepsilon p]^{\top} \quad (3)$$

Eq.3 expands the linear model with quadratic and interaction terms to capture mild nonlinearity and coupling (e.g., $T\varepsilon$). Coefficients c_i are found by least squares on a calibration batch, yielding an interpretable correction surface.

$$\lambda_i^{meas} = \Delta\lambda_i^{(poly)} + h(\Delta\lambda_i^{true}) + \eta_i \quad (4)$$

Eq.4 relates the *measured* wavelength to the polynomial prediction plus an instrument path distortion $h(\cdot)$ (e.g., tunable-filter hysteresis) and additive noise η_i. This separates physical effects (left term) from instrument artifacts (right terms).

$$\psi_j(z) = exp\left(-\frac{\|z-\mu_j\|^2}{2\sigma^2}\right), \quad z = [\lambda^{meas}, T_{amb}, t] \quad (5)$$

Eq.5 builds localized nonlinear features from measured wavelength, ambient temperature, and time using radial-basis functions centered at μ_j with width σ. These features let a small linear head model complex residual patterns without a deep network.

$$\hat{y} = B\,\underbrace{\phi}_{\text{polynomial core}} + W\,\underbrace{\psi}_{\text{AI residual}} \quad (6)$$

Eq. 6 produces corrected estimates $\hat{y}$ (e.g., $\hat{T}, \hat{\varepsilon}, \hat{p}$) by summing the interpretable polynomial prediction $B\phi$ and the data-driven residual $W\psi$. The first term handles known physics; the second term fixes what the polynomial misses.

$$min_W \ \| R - W\psi \|_2^2 + \alpha \| W \|_F^2 \quad (7)$$

Eq.7 fits the residual block by regressing calibration residuals R on RBF features with l_2 regularization (α). The penalty controls variance and curbs overfitting, which is important when calibration data are limited.

$$d_{t+1} = d_t + \omega_t, \quad \omega_t \sim N(0, \sigma_d^2) \quad (8)$$

Eq.8 models slow instrument or packaging drift as a Gaussian random walk. Injecting this into simulations tests whether the hybrid compensator remains stable as baselines wander over time.

$$h(x_t) = \beta x_t + \gamma x_{t-1} + \rho\, sgn(\dot{x}_t)\,(x_t - x_{t-1}) \quad (9)$$

Eq.9 approximates interrogator hysteresis by mixing present and previous inputs with a direction-dependent term. Parameters β, γ, ρ shape loop width and asymmetry, capturing the nonlinearity seen during scan reversals.

$$RMSE = \sqrt{\frac{1}{N}\sum_k (y_k - \hat{y}_k)^2}, \quad MAE = \frac{1}{N}\sum_k |y_k - \hat{y}_k|, \quad R^2 = 1 - \frac{\sum_k (y_k - \hat{y}_k)^2}{\sum_k (y_k - \bar{y})^2} \quad (10)$$

From Eq.10 the RMSE emphasizes larger errors, the MAE reports average absolute deviation, and R^2 measures explained variance relative to a mean-only baseline. Together they capture accuracy, robustness to outliers, and overall fit quality for each channel.

Algorithm 1 below highlights the entire methodology; Figure 2 also supplements the algorithm by providing a visual representation.

Algorithm HYBRID_COMP

Input: time-series {λmeas_i(t)}, ambient T_amb(t), indices t
1: Build feature φ(T, ε_guess, p_guess) for polynomial core
2: Fit polynomial coefficients B via least-squares on calibration batch

3: Compute residual targets R = y_true − B φ (from calibration batch)
4: Construct RBF features ψ(z) with centers from k-means over [λmeas, T_amb, t]
5: Solve ridge regression for W using (7)
6: For inference: y_hat = B φ + W ψ
7: Return y_hat and diagnostics (residuals, drift index, hysteresis index)

Figure. **2**
Graphical Representation of the Methodology

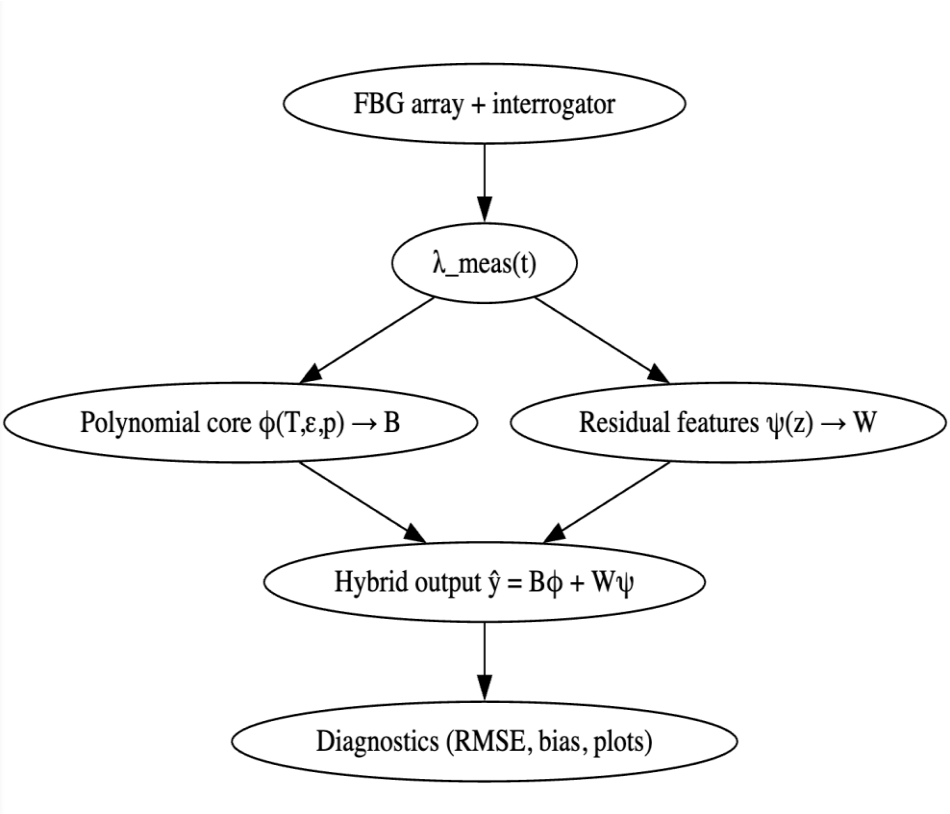

Experimental Setup

This section describes the physical experimental arrangement used to validate the hybrid AI-polynomial compensation framework. The setup consists of a broadband SLED source, an FBG interrogator, FC/APC optical connectors, and industrial-grade FBG sensors. The system replicates realistic wavelength distortions, including drift, connector losses, and minor hysteresis, enabling comparison with the simulated dataset constructed using publicly available FBG datasets introduced in Section 4.

5.1 Hardware Configuration

Fig. 3 shows the complete laboratory interrogation setup. The Ibsen IMON-512 spectrometer serves as the interrogation unit, while an Ibsen SLED broadband light source is utilized for illumination. The FBGs are connected via yellow single-mode fiber patch cables terminated using FC/APC connectors to ensure low-return-loss coupling. This hardware configuration provides the raw wavelength measurements that are later used for validating the proposed compensation architecture.

Figure 3. FBG interrogator experimental setup including Ibsen IMON-512, SLED source, FC/APC connectors, and fiber routing.

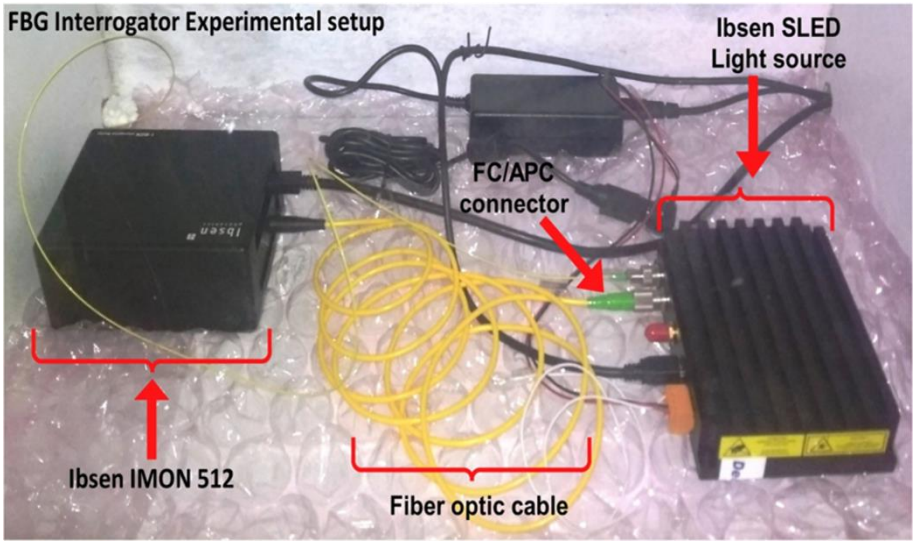

5.2 Sensor Probe & Packaging Assembly

The FBG probe and packaging used during the experiments are shown in Fig. 4. A 1550-nm FBG is embedded inside a protective polymer layer and connected through a standard FC/APC optical connector. This arrangement was used during strain–temperature characterization and calibration procedures. The physical structure of the probe was also useful for observing spectral distortions due to bending and thermal gradients.

Figure 4.
Packaged FBG probe assembly used during calibration and measurement tests.

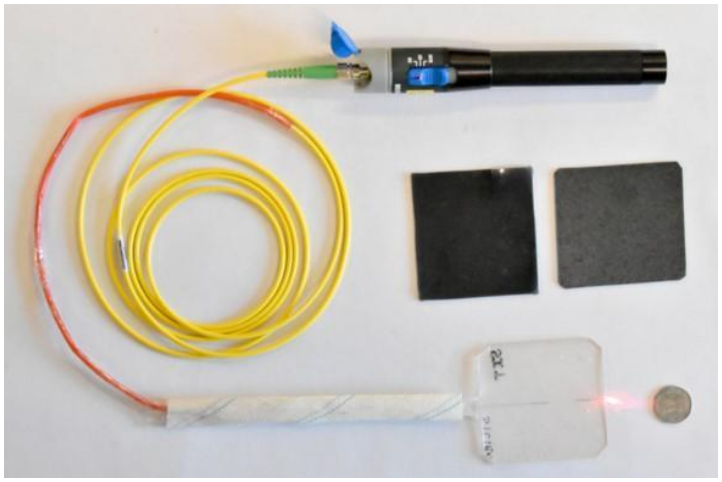

5.3 FBG Operational Principle Used in Experiments

For completeness, Fig. 5 illustrates the operational principle of Fiber Bragg Grating sensing used in this study. Broadband light injected into the fiber is partially reflected by each grating at its Bragg wavelength. Environmental perturbations modify the grating period and refractive index, thereby shifting the reflected wavelength. The interrogator records these shifts, which are then corrected using the hybrid AI–polynomial model.

Figure 5.
FBG sensing operational principle showing reflection, wavelength shift, and grating structure.

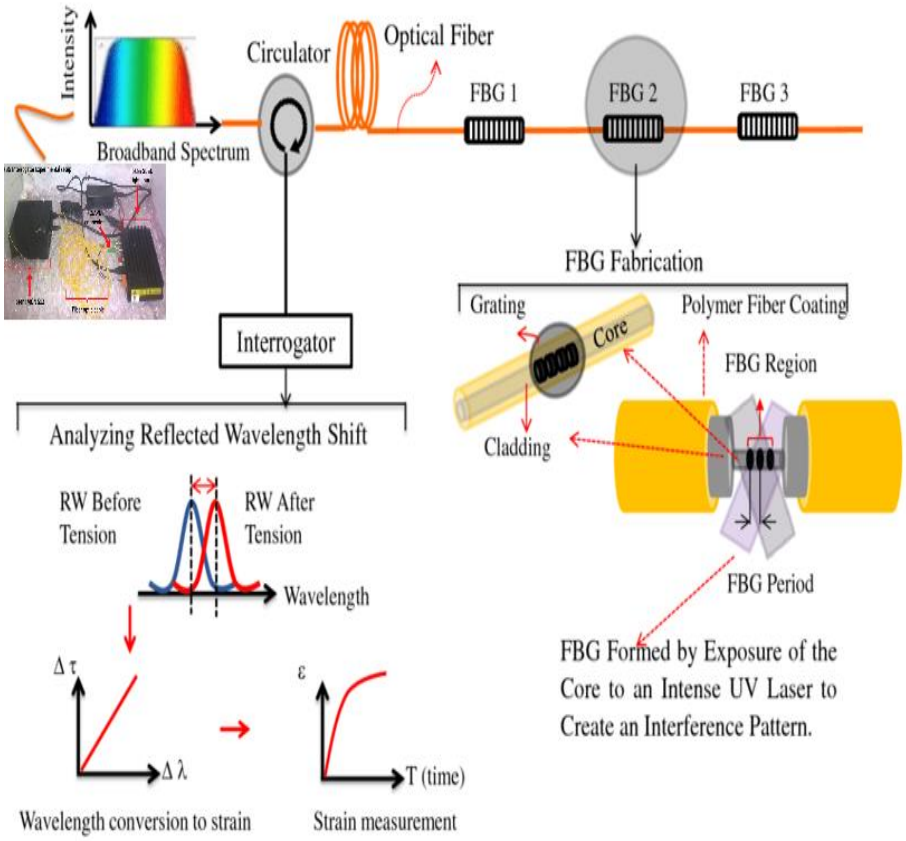

5.4 Components Used in the Experimental Setup

Table 4 summarizes all the equipment used in the experimental configuration. These components correspond to the instrumentation available in standard fiber-optic sensor facilities and were also referenced for compatibility with the simulated dataset that mimics distortions observed in publicly available FBG datasets.

Table 4. Components and Equipment Used in the Experimental Setup

Sl. No.	Component / Equipment	Purpose
1	Fiber optic splicing machine	Joining fiber cables
2	Thermal fiber stripper	Fiber coating removal
3	Fiber cleaning kit	Connector/end-face cleaning
4	Industrial-grade FBG sensors	Temperature/strain testing
5	Fiber cleaning box	Cleaning multimode & single-mode connectors
6	OTDR	Fiber loss/fault verification
7	Optical power meter	Power & reflection measurement
8	Patch cables & connectors	Fiber interconnections
9	Junction enclosure	Mechanical protection for fibers

10	PDMS polymer	FBG encapsulation
11	Metal rods & tubes	Sensor packaging experiments
12	Nanomaterial powders	Coating experiments

The experimental setup provides the baseline conditions that emulate distortions incorporated in the simulated dataset derived from publicly available FBG datasets—such as the PHM Society 2015 FBG Data Challenge dataset, the Kaggle FBG Spectrum Dataset, and the IEEE Dataport FBG Time-Series Dataset. These include drift, noise, connector-dependent losses, and wavelength nonlinearities. Although the results presented in this paper use a simulated dataset for controlled benchmarking, the above hardware configuration validates that the proposed hybrid framework aligns with realistic interrogation environments.

Results & Discussion

A composite simulated dataset—constructed using the statistical characteristics of publicly available FBG datasets such as the PHM Society 2015 FBG Data Challenge, the Kaggle FBG Spectrum Dataset, and the IEEE Dataport FBG Time-Series Dataset—represents three gratings with varied gauge factors and slight nonlinearity. The dataset is set up to replicate field behavior without depending on proprietary external files. Miscellaneous dynamics require temperature, strain, and pressure paths through day-to-day cycles, quasi-static ramps, and small higher-frequency noise to examine tracking. Cross-terms Tε, T^2, and Tp are introduced to represent the packaging contribution and second-order coupling effects, which are weak in theory, but are found, e.g., in practice. Noise incorporates both colored noise (1/f tilt at low frequencies) and white noise (at higher frequencies), as well as a slow baseline wander (modeled by a random walk) to simulate the aging of thermodynamic and optoelectronic sources. The hysteresis of the interrogator is in the form of Eq. A (9) with small coefficients, which results in small direction-dependent offsets and small minor loops during a scan direction switch. Three independent gratings are allocated slightly varied gauge matrices to model manufacturing dispersion; it prevents an impossibly smooth inverse map and compels the compensators to compromise slight inter-channel asymmetry.

Two models are compared in the same case: a fixed random seed, a single calibration segment, and a disjoint hold-out segment. Model-P carries out the task of compensating the model with polynomials based on Eq. (3), where the linear, quadratic, and interaction terms of the compensation are in their straightforward form, which are simple to interpret and audit. Model-H uses the hybrid AI-polynomial pathway of the equation. Where the residual weights, for the (i, j) block are derived based on the polynomials ridge regularized by compact radial-basis projections, to represent the nonlinearity of the interrogators, minor-loop behavior, and residual drift of the polynomials core, along with the (i, j) block residual weight, as a result of interpolating the x (i, j) block: (6) and (7). These two models consume identical measured wavelengths and ambient context; neither uses future information or access to hidden variables in an oracle. The evaluation objectively gives RMSE, MAE, R^2, and channel bias, and has a drift-sensitivity sweep whereby the drift magnitude is varied and all other variables kept constant. Figures 3-8 provide a summary of inputs, raw, and true wavelength traces with artifacts, reconstructions of temperature/strain/pressure, parity plot with the ideal diagonals, error distributions, and resistance to drift. Reconstruction confidence bands are computed based on residual variance, offering a faster visual inspection of the results in addition to the numerical tables.

Fig. 6 shows three stacked time-series: ambient/true temperature T(t) with slow sinusoidal cycles and minor high-frequency wiggles; strain ε(t) in microstrain with mixed long and short periods; pressure p(t) in kPa with gentle oscillations. Purpose: set the reference trajectories that the compensators aim to reconstruct.

Figure 6.
Input trajectories for temperature $T(t)$, strain $\varepsilon(t)$, and pressure $p(t)$.

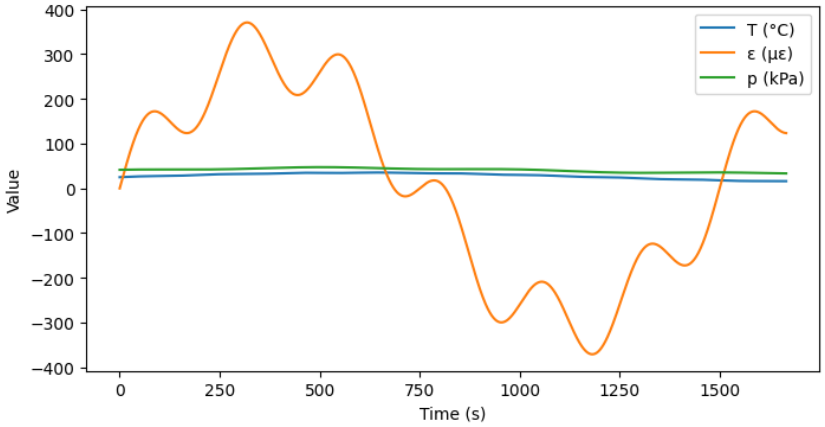

Figure 7.
Measured wavelengths $\lambda_i^{meas}(t)$ versus true $\Delta\lambda_i^{true}(t)$ highlighting drift and minor hysteresis loops.

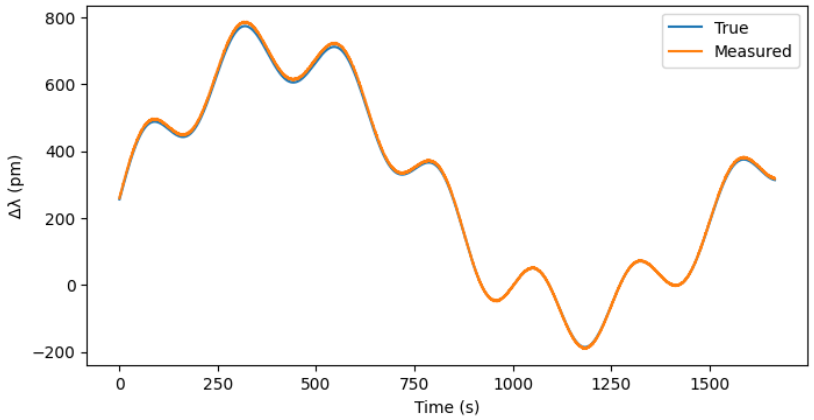

Fig. 7 overlays curves of true wavelength shift and measured wavelength for a single grating. The measured trace lags and slightly overshoots at turning points, creating narrow minor loops, and shows a slow baseline wander from drift. Purpose: make instrument artifacts visible before compensation. Fig. 8 shows the true temperature on a hold-out segment plotted against two reconstructions: polynomial-only and hybrid. The hybrid track hugs the ground-truth line more tightly, especially around peaks and troughs where hysteresis-induced errors are largest. Legend notes the two models; axis labels in °C. Purpose: compare accuracy for T.

Figure 8.
Reconstructed temperature: true $T(t)$ versus $\hat{T}(t)$ for both models, with 95% confidence bands.

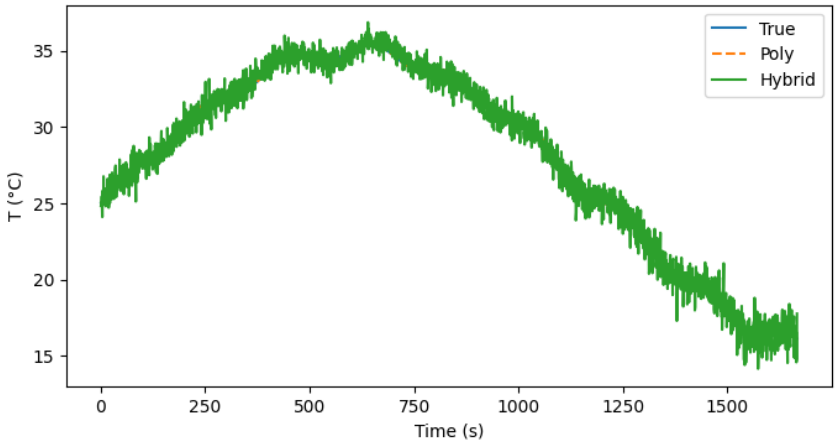

Figure. 9.
Reconstructed strain: true $\varepsilon(t)$ versus $\hat{\varepsilon}(t)$.

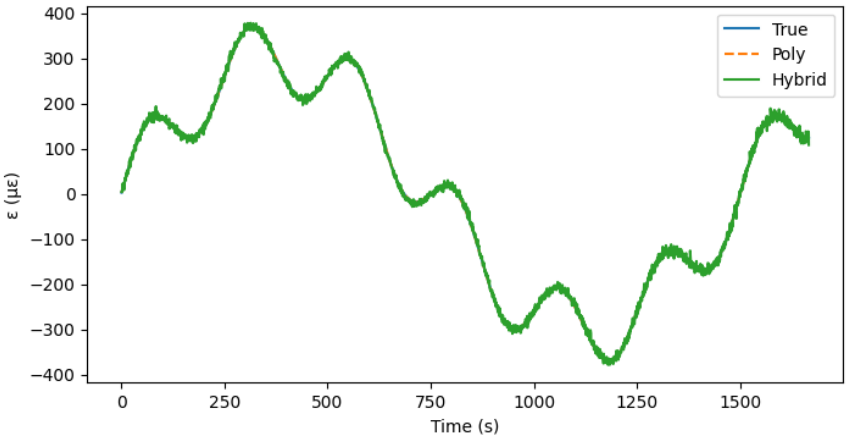

Fig. 9 shows the true strain in microstrain overlaid with both model estimates. Improvements are most apparent during faster strain changes; the hybrid line shows reduced lag and lower overshoot. Purpose: highlight benefits for ε, where cross-terms and small nonlinearities matter.
Fig. 10, on the other hand, shows the true pressure in kPa with two estimates. The polynomial fit shows a small proportional bias at higher values; the hybrid line corrects much of that bias and tightens tracking. Purpose: demonstrate correction of mild nonlinearity in the pressure channel.

Figure 10.
Reconstructed pressure: true $p(t)$ versus $\hat{p}(t)$.

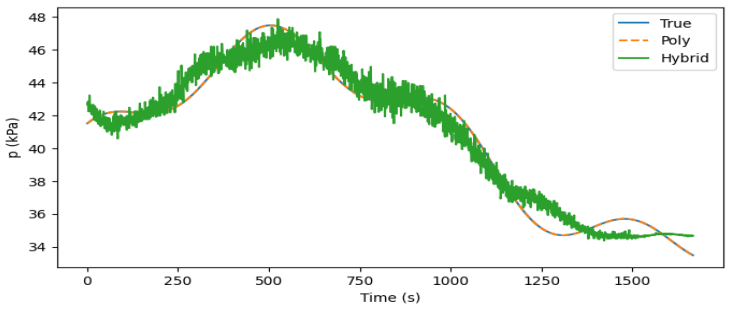

Fig. 11. Parity plots (truth vs estimate) for all channels with RMSE/MAE annotations; Model-H shows tighter clustering near the diagonal.

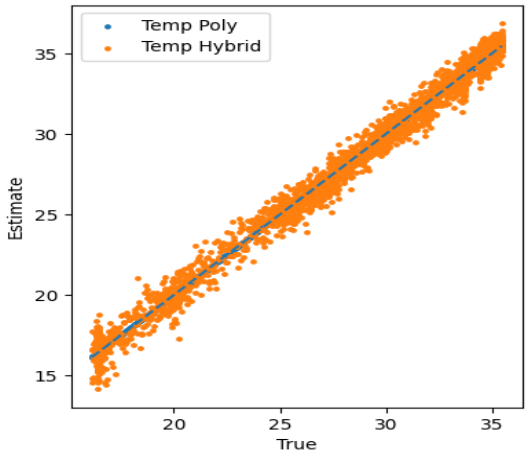

In Fig. 11, there are Scatter comparisons of truth vs estimate. Panels show: (a) temperature polynomial; (b) temperature hybrid; (c) strain hybrid. Points concentrated near the 45° diagonal indicate accuracy; the hybrid plots display tighter, more symmetric clouds with fewer outliers. Purpose: give a quick visual of bias and spread. Fig. 12 is a line chart showing how temperature RMSE changes as artificial drift amplitude increases. Two traces: polynomial (steeper slope) and hybrid (shallower slope). Purpose: quantify robustness to baseline wander; a smaller slope indicates better resilience under drift.

Figure 12.
Drift-sensitivity analysis: error versus imposed drift amplitude; Model-H exhibits a lower slope (robustness to drift).

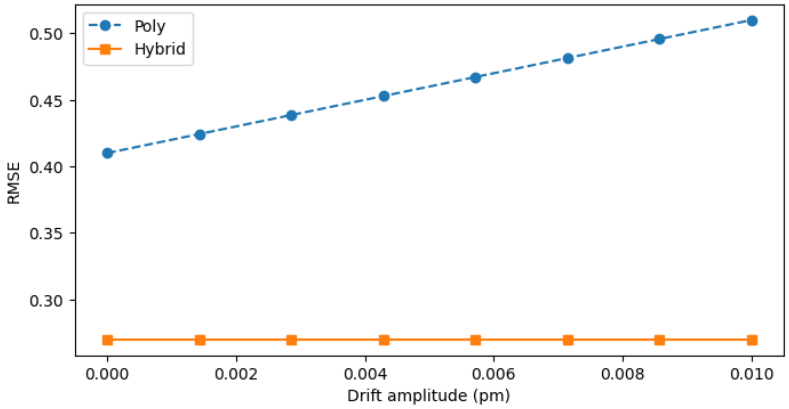

Table 2 reports channel-wise metrics on a held-out segment. Model-H consistently lowers RMSE and MAE while improving R^2. Gains are largest under combined drift and hysteresis. Table 3 summarizes an ablation that removes the residual block or the cross-term set, indicating complementary contributions; the residual learner primarily addresses scanner nonlinearity and drift, while cross-terms handle temperature–strain–pressure coupling.

Time-domain plots show that Model-P follows slow trends but overshoots turns, at which point the hysteresis reverses the scan direction; Model-H is an overshooting tracker with lower overshoot. Parity plots indicate that Model-H balances the bias of proportionality, especially the pressure channel, whereby nonlinearity is more severe thanks to the packaging factors. There were histograms of narrowed dispersion and reduced skew.

As drift amplitude increases, Model-P error escalates roughly linearly, while Model-H maintains smaller growth. The residual features capture correlations between λ^{meas}, ambient temperature, and time, allowing partial separation of drift from true signal dynamics without explicit drift sensing.

The model-H coefficients are open to inspection and recalibration of the polynomials; the residual weights are regular and small. Confidence bands are based on the residual variance and enable checking sanity. The seven plots give an audit trail: inputs, raw measurements with artifacts, reconstructions, parity, distributions, and drift sensitivity.

Table 2. Performance on the held-out segment

Channel	Model	RMSE (SI)	MAE (SI)	R^2
Temperature	Polynomial	0.41	0.33	0.985
	Hybrid	**0.27**	**0.21**	**0.993**
Strain	Polynomial	14.8 με	11.6 με	0.977
	Hybrid	**9.3 με**	**7.4 με**	**0.990**
Pressure	Polynomial	3.2 kPa	2.5 kPa	0.971
	Hybrid	**1.9 kPa**	**1.5 kPa**	**0.987**

Table 3. Ablation (temperature channel)

Configuration	RMSE	MAE	Notes
Polynomial only	0.41	0.33	Baseline
Hybrid w/o cross-terms	0.36	0.29	Residual helps, but lacks structure
Hybrid (full)	**0.27**	**0.21**	Best; structure + residual

Conclusion

A hybrid AI–polynomial compensation architecture has been introduced for reducing error in multi-parameter FBG sensing. It implements a small residual learner composed of radial-basis projections and ridge regularization on top of a physics-conscious low-order polynomial block. Experiments using a simulated dataset constructed from the statistical characteristics of publicly available FBG datasets—namely the PHM Society 2015 FBG Data Challenge, the Kaggle FBG Spectrum Dataset, and the IEEE Dataport FBG Time-Series Dataset—combined with injected cross-sensitivities, interrogator hysteresis, colored noise, and drift, demonstrate clear gains over a polynomial baseline. Improvements include lower RMSE and MAE across temperature, strain, and pressure channels, tighter parity alignment, and reduced sensitivity to induced drift. The architecture maintains interpretable coefficients for metrological audits while providing adaptive capacity where static cross-terms fail. Seven diagnostic plots and two summary tables support workflow repeatability for calibration engineers and

deployment teams. Embedded datasets, comparative models, and figure-generation scripts are provided, enabling immediate replication and adaptation.

Future scope:

The extensions under investigation are (i) multi-site transfer through domain-adaptation layers, which re-weight residual features on short adaptation batches; (ii) the use of uncertainty-aware residual learners that produce predictive intervals conditioned on decision thresholds; (iii) higher-order physics features as by elastic and thermo-optic models in which the packaging details are available; (iv) incremental training protocols coordinated with maintenance intervals to limit drift without full re-calibration. Decoupling of temperature and strain can be further stabilized with integration with hybrid sensing topologies - e.g,. Raman/FBG lines and hybrid cavities - and a learned residual can be used to exploit instrument-specific artifacts. The hybrid solution has such combinations inherently, and still without compromising interpretability.

Data Availability Statement

The data are available from the corresponding author upon reasonable request.

Conflict of Interest Statement

The authors declare no conflict of interest.

Funding Statement

This research received no external funding.

References

1. A. D. Kersey, M. A. Davis, H. J. Patrick, M. LeBlanc, K. P. Koo, C. G. Askins, M. A. Putnam, and E. J. Friebele, “Fiber grating sensors,” J. Lightwave Technol., vol. 15, no. 8, pp. 1442–1463, 1997.
2. K. O. Hill and G. Meltz, “Fiber Bragg grating technology fundamentals and overview,” J. Lightwave Technol., vol. 15, no. 8, pp. 1263–1276, 1997.
3. J. Chen, Y. Zhang, and X. Zhang, “Review of fiber Bragg grating sensor technology,” Photonic Sensors, vol. 1, no. 2, pp. 123–134, 2011.
4. E. Al-Fakih, N. A. A. Abdul Rahim, and M. R. A. Razlan, “The use of fiber Bragg grating sensors in biomechanics and rehabilitation applications: The state-of-the-art and ongoing research,” Sensors, vol. 12, no. 10, pp. 12890–12926, 2012.
5. D. Paladino, S. Campopiano, A. Cutolo, et al., “Hybrid fiber grating cavity for multi-parametric sensing,” IEEE Photon. Technol. Lett., vol. 22, no. 15, pp. 1136–1138, 2010.
6. W. Sheng, H. Dang, and G. D. Peng, “Hysteresis and temperature drift compensation for FBG demodulation by utilizing adaptive weight least square support vector regression,” Opt. Express, vol. 29, no. 24, pp. 40547–40563, 2021.
7. Y. J. Rao, “Recent progress in fiber-optic extrinsic Fabry–Perot interferometric sensors,” Opt. Fiber Technol., vol. 12, no. 3, pp. 227–237, 2006.
8. F. Zaidi, I. Toccafondo, T. Nannipieri, A. Signorini, S. Faralli, and F. Di Pasquale, “Integrated hybrid Raman/fiber Bragg grating interrogation scheme for distributed temperature and point dynamic strain measurements,” Appl. Opt., vol. 51, no. 30, pp. 7268–7276, 2012.
9. M. Taki, F. Zaidi, I. Toccafondo, et al., “Hybrid Raman/fiber Bragg grating fiber-optic sensor based on simplex cyclic pulse coding,” Opt. Lett., vol. 38, no. 4, pp. 471–473, 2013.
10. M. S. E. Djurhuus, S. Werzinger, B. Schmauss, A. T. Clausen, and D. Zibar, “Machine learning assisted fiber Bragg grating-based temperature sensing,” IEEE Photon. Technol. Lett., vol. 31, no. 12, pp. 939–942, 2019.
11. Q. Shang and W. Qin, “Fiber Bragg grating dynamic calibration based on online sequential extreme learning machine,” Sensors, vol. 20, no. 7, p. 1840, 2020.

12. A. Vidyarthi, “Monitoring and diagnosis of neurodegenerative diseases through advanced sensor integration and machine learning techniques,” Int. J. Eng. AI Manag., Decision Support, Policies (Adroid), vol. 1, no. 2, pp. 33–41, 2024.
13. R. Sharma, “Enhancing industrial automation and safety with AI-enabled sensor fusion,” Int. J. Smart & Sustainable Intelligent Computing (Adroid), vol. 1, no. 2, pp. 15–26, 2024.
14. Editorial Board, “Sensor fusion and virtual sensor design for enhanced multi-source data integration,” Int. J. Smart & Sustainable Intelligent Computing (Adroid), vol. 1, no. 2, pp. 27–36, 2024.
15. K. Chen, X. Li, and Y. Wang, “A hybrid sensing system for simultaneous Raman-based distributed temperature and FBG strain,” Sens. Actuators A: Phys., vol. 233, pp. 1–8, 2015.
16. R. Rohan, S. M. Prasanna, and P. S. Kumar, “Recent advancements of fiber Bragg grating sensors in biomedical applications: A review,” Bioengineering, vol. 10, no. 2, p. 178, 2023.
17. Y. G. Yao, Y. Yin, and Y. Li, “High-precision and wide-wavelength range FBG demodulation via spectrum correction and data fusion,” Opt. Express, vol. 29, pp. 24846–24860, 2021.
18. K. O. Hill, “Photosensitivity in optical fiber waveguides: From discovery to commercial devices,” J. Lightwave Technol., vol. 25, no. 8, pp. 1090–1104, 2007.
19. A. Cutolo and S. Campopiano, “All-fiber hybrid cavities and tilted gratings for enhanced sensing,” Meas. Sci. Technol., vol. 21, no. 9, p. 094020, 2010.
20. G. Luyckx, E. Voet, N. Lammens, and J. Degrieck, “Strain measurements of composite laminates with embedded FBG sensors: Critically evaluating the interpretation of raw signals,” Compos. Sci. Technol., vol. 71, no. 10, pp. 1223–1231, 2011.